Synthesis, surface chemical analysis, lifetime studies and degradation mechanisms of Cs-K-Sb photocathodes

H. Panuganti *, E. Chevallay, V. Fedosseev, M. Himmerlich

The European Organization for Nuclear Research (CERN), 1211 Geneva 23, Switzerland

ABSTRACT

We report synthesis and characterization of a batch of three cesium potassium antimonide photocathodes that have been grown on pure copper substrates via a ternary co-deposition method whose procedure is described herein. A deposition system that was designed for synthesis of two-element photocathodes has been utilized for synthesis of the aforementioned three-element photocathodes with slope of the in situ photocurrent as the driver for the growth process. A variation of substrate temperature and deposition parameters among the three photocathodes during synthesis has yielded a maximum quantum efficiency of 6% for 140 °C substrate temperature. Lifetime studies performed in a 65-kV DC electron gun on two of the photocathodes, but under oxidized states, at tens of μA average currents (ampere-level peak currents) extracted utilizing a 532-nm wavelength, 1-kHz repetition rate laser, have resulted in charge-lifetimes of 6.13 C and 13.78 C, respectively. X-ray photoelectron spectroscopy analysis of the photocathode with the highest quantum efficiency has revealed a nearly impurity-free surface with stoichiometry $Cs_{1.3}K_{1.8}Sb_{1.0}$ when pristine. Furthermore, it has been found that oxidation of the alkali surface atoms as well as carbon adsorption from hydrocarbons and minor fluorine uptake are the causes of quantum efficiency reduction during laser illumination in the utilized experimental set-up.

1. Introduction

Semiconductor photocathodes are widely used for electron beam generation in particle accelerators, owing to their characteristics like high quantum efficiencies (QEs), reasonable lifetimes and sub-picosecond to picosecond response times [1]. However, popular semiconductor photocathodes like cesium telluride (Cs-Te) and most metallic photocathodes require ultra-violet (UV) lasers to generate electron beams with reasonable charge [2]. The typical generation of ultra-short UV laser pulses is achieved from a two-stage frequency up-conversion of high pulse energy (often in the mJ level) solid-state infrared (IR) lasers, an inefficient process that has additional limitations like pulse-to-pulse energy stability in some cases of high intensity and repetition rate pulse trains [3]. As a plausible solution, gallium arsenide (Ga-As) photocathodes have creditable QEs (~10%) in the visible spectral range while having a non-trivial (~1%) QE distribution in the near-IR (<1 μm) spectral region [4,5]. However, they have considerably slower response times (tens of ps) [1,6,7] and their requisite surface activation layers are fragile under radiofrequency (RF) gun environments [8].

Alkali antimonide semiconductor photocathodes exhibit appreciable QEs in the green section of the laser spectrum whose generation can be achieved by a single stage frequency doubling of the aforementioned IR lasers, thus leading to higher wall-plug efficiencies, drive laser pulse-to-pulse energy stability and simpler apparatus. Ever since their first realization, multialkali antimonide photocathodes have been generally found to have greater photosensitivity in the visible spectrum compared to their monoalkali counterparts. Bialkali antimonides draw great interest since their performance is comparable to trialkali antimonides (for <600-nm drive laser wavelengths), but are substantially simpler and economical to synthesize [9–11].

Cesium potassium antimonide (Cs-K-Sb (stoichiometrically independent representation)) photocathodes are well-known from the photomultiplier industry due to their high QEs and very low thermionic dark currents [12,13]. They are routinely synthesized at photoemission laboratories across the world, with QEs of up to ~10% in the green laser spectrum. With prompt response times suitable for certain fast streak camera applications and capabilities of delivering ampere-class currents [14], Cs-K-Sb photocathodes make attractive candidates for the current and next generation electron accelerators like free-electron lasers [15] and energy recovery linacs [14,16] that require ultra-short, high brightness [17,18] and high current electron beams.

Despite their significant advantages, Cs-K-Sb photocathodes are yet to be developed into mainstream photocathodes of choice for the next generation accelerators because of some setbacks like their poor

---

tolerance to RF gun environments. Although recognized as prompt, it is not known whether Cs-K-Sb photocathodes can deliver sub-picosecond bunches that are desired in, for instance, ultra-fast electron diffraction applications [19,20]. Consequently, a considerable amount of research has in recent times been invested in improving the lifetime of such photocathodes along with the development of other relevant attributes like QE.

Under the framework of the Compact Linear Collider (CLIC) project design study [21–23], a photoinjector option for the CLIC drive beam provides better control in the time structure of the electron bunches over the thermionic emitter and bunching system where formation of undesired satellite bunches increases beam loss and radiation [3,24, 25]. However, the photoinjector option imposes stringent requirements on the photocathode, such as charge extraction of ∼8 nC per micro-bunch at 500 MHz (50 Hz) micro-bunch (macro-bunch) repetition rates. The required bunch charge and drive laser stability of <0.1% (rmsd) calls for consideration of alkali antimonides operated in the green laser spectrum. Previously conducted studies on Cs-Sb photocathodes under the framework of the CLIC drive beam generation have been reported elsewhere [26–28] where synthesis optimization to obtain proper stoichiometry and controlled testing in RF environments remains to be explored. In the same direction, utilization of Cs-K-Sb photocathodes may provide higher beam brightness when compared to other photocathodes that operate in the green laser spectrum, which motivated the current study.

Direct comparison of the properties of photocathodes manufactured and studied at various laboratories is difficult due to notable variations in the fabrication procedures, apparatus and measurement techniques [29]. The primary intention of the current work is to develop a reliable fabrication process of Cs-K-Sb photocathodes utilizing our physical vapor deposition system that was originally designed for two-element deposition, estimate the charge-lifetime, and study via X-ray photoelectron spectroscopy (XPS) the surface chemical properties and the processes that contribute to photocathode degradation. Co-deposition methods, sometimes referred to as simultaneous deposition methods, were chosen since they can offer more photosensitive photocathodes due to possible reduction of contamination of the otherwise sequential layers, from residual gases before cathode formation [30]. Ternary co-deposition methods have also been shown to yield better QE, photocathode surface roughness and fabrication reproducibility [31,32].

The following sections describe the apparatus, procedures, and experimental results of the current research. Section 2 describes the experimental set-up, including that of the photoemission and XPS laboratories. Section 3 discusses the synthesis procedure utilized to fabricate three Cs-K-Sb photocathodes. Charge-lifetime studies conducted on two of the photocathodes under oxidized conditions are reported in Section 4. Section 5 details the XPS analysis performed on the photocathode with the highest QE (6%) before and after the measurement of charge-lifetime. Finally, Section 6 summarizes the results with a future outlook.

2. Experimental set-up

2.1. Photoemission laboratory

CERN's photoemission laboratory [33] includes a photocathode preparation chamber equipped with a physical vapor deposition system originally designed for two-element deposition, and a test DC electron gun beamline for photocathode characterization as shown in Fig. 1. A transfer arm mechanism allows for a quick photocathode transfer from the preparation chamber to the DC gun sans vacuum intervention. The lab is equipped with two commercial flash-lamp pumped Q-switched Nd:YAG[1] laser systems which deliver up to 10 kHz (QUANTRONIX model
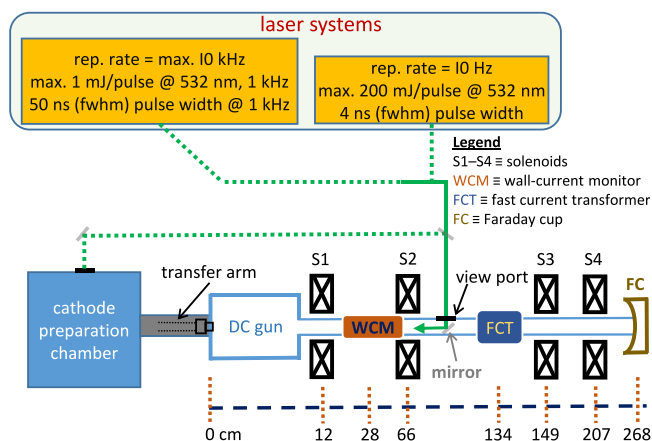

Fig. 1. A schematic (not to scale) of CERN's photoemission laboratory's preparation chamber, DC gun beamline and laser systems, with only the relevant components shown.

532 DP-1) and 10 Hz (SPECTRON model SL802) repetition rate pulse trains, respectively. Either laser system can generate laser pulses of wavelength 532 nm via a single stage second-harmonic frequency up-conversion of the source 1064-nm IR using a DCDA[2] crystal, or 266-nm UV pulses via an additional second-harmonic stage using a KDP[3] crystal; Fig. 1 shows some additional laser pulse specifications. The laser light is directed onto the photocathode in the preparation chamber for in situ photocurrent measurement during the synthesis process, or directed into the DC gun for photocathode characterization, using the respective sets of vacuum viewports and protected-aluminum mirrors (see Fig. 1).

The operational voltage of the DC gun is 65 kV. For proper transport of the electron beam that exits the gun, four solenoidal magnets S1–S4 are employed along the beamline for weak focusing, as shown in Fig. 1. When not in operation, the vacuum pressure in the photocathode preparation chamber and in the beamline is typically maintained below 4×10^{-11} mbar, while the DC gun is maintained below 1×10^{-11} mbar, by utilizing several ion pumps and titanium sublimation pumps. Four vacuum gauges, two in the preparation chamber and one each in the gun and the beamline, monitor the corresponding pressures. A wall-current monitor (WCM) with an acceptance bandwidth from 1 MHz to 10 GHz [34] located between S1 and S2 (see Fig. 1) records the generated electron beam current for bunches with durations on the order of 10 ns. For longer bunches, a fast current transformer (FCT) or a Faraday cup (FC) located at the end of the beamline is utilized for beam charge measurements. A residual gas analyzer (RGA) system is installed in the preparation chamber in order to monitor for any gaseous contaminants.

The photocathode preparation chamber is designed for co-deposition methods on the grounds of historical success of such methods in producing better QE and lifetime Cs-Te photocathodes [33,35, 36] at the facility, in comparison to the more traditional sequential-layered deposition methods. The chamber contains three dispensers corresponding to Cs, K and Sb as shown in Fig. 2(b). The Sb dispenser is homemade from a molybdenum crucible and consists of pure Sb with impurities ≤1×10^{-4}%. The wire-shaped alkali dispensers (SAES GETTERS S.P.A) consist of the respective alkali chromates with Zr-Al (St 101 alloy) reducing agents, which release pure alkali vapors when heated to correct temperatures. Each dispenser bears a dedicated power supply for an independent control of the associated evaporation rate via resistive heating. A total of three Cs-K-Sb photocathodes can be synthesized on average before exhausting the dispensers. The reloading
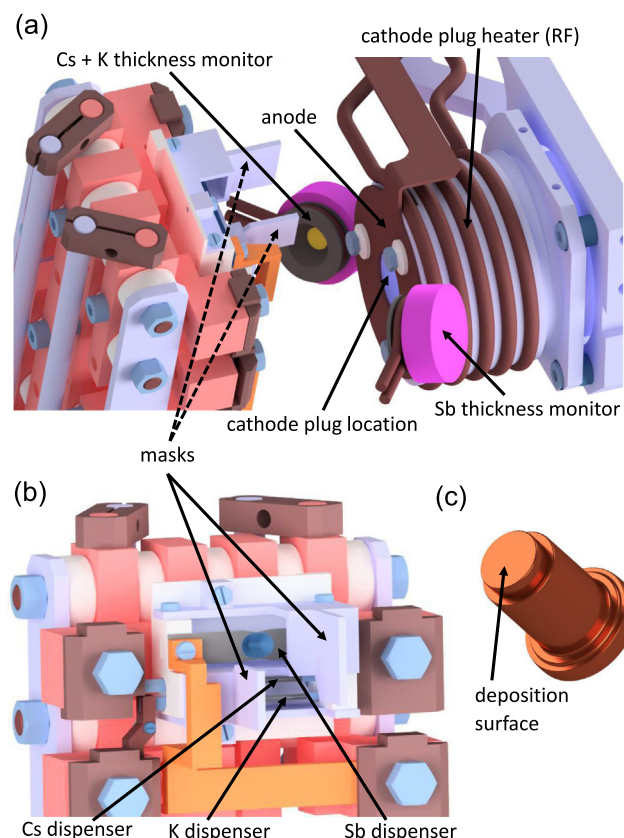

Fig. 2. Computer-aided renderings of the internal cathode preparation chamber (perspective views) depicting the thickness monitors, anode and the substrate heater (a), and the element dispensers and masks (b). The copper cathode plug is shown in (c). Scaling information for (a): direct distance between the center of the Sb dispenser and the cathode plug center is ~55 mm.

procedure of the dispensers involves venting the preparation chamber to atmospheric pressure, reloading, and baking the main components at 150 °C for approximately four days including temperature ramp-up and ramp-down times. In parallel, the vacuum pumps and the RGA instrumentation are baked at 300 °C and 330 °C, respectively. There are two deposition-thickness monitors (quartz microbalances), as shown in Fig. 2 (a), that respectively monitor the deposited thicknesses from the two sets of dispensers corresponding to alkali metals (collectively) and Sb. The independent thickness-monitoring is achieved by a pair of masks that shield the alkali thickness monitor from Sb vapor and vice versa. The preparation chamber can accommodate a maximum of three cathode plugs at any given time including two storage positions.

The 19-mm diameter top surface of an oxygen-free electronic (OFE) grade copper cathode plug (Fig. 2 (c)) with oxygen content $<5 \times 10^{-4}\%$ serves as the substrate; the substrate preparation is described in Section 3. The cathode plug is inserted in a receptacle that is equipped with an RF heater that facilitates control of the substrate temperature between room temperature and 200 °C as measured by a thermocouple. The thermocouple is in thermal contact with the receptacle whose temperature is assumed to represent the temperature of the cathode plug. During a deposition process, the generated photoelectron current can be monitored in real time for QE optimization with a circular anode (Fig. 2 (a)) biased at 1 kV with respect to the cathode potential. The direct distance between the cathode surface and the central plane of the anode is ~3 mm. A shutter located between the dispensers and the substrate allows for a precise control of the start and stop times of the deposition process onto the substrate. The remote control, monitoring and data acquisition of critical parameters like dispenser currents, deposition thicknesses and photocurrent is achieved via the equipped
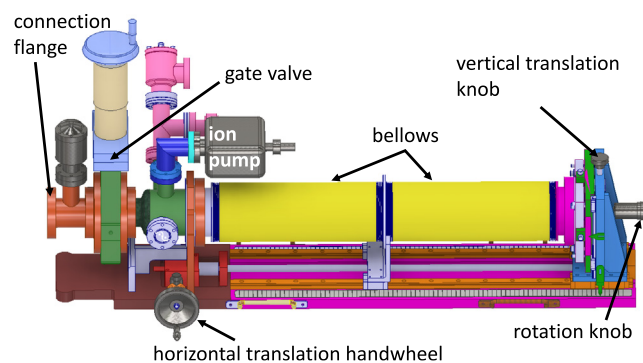

Fig. 3. A computer-aided drawing of the UHV transfer vessel (perspective view).

software interfaces written in C (processing) and JAVA (user interface). A motorized mirror located outside of the beamline allows for an automated QE scanning at discrete planar points on the photocathode surface.

2.2. XPS laboratory

A commercial ultra-high vacuum (UHV) system (SPECS SURFACE NANO ANALYSIS GMBH, Berlin, Germany) is utilized for XPS characterization of photocathodes. The system consists of a hemispherical electron energy analyzer with 9 channeltrons (PHOIBOS 150) and a monochromated Al-K$_\alpha$ X-ray source (XR50M, $h\nu = 1486.7$ eV). While the base pressure of the system is below 2×10^{-10} mbar, the pressure is maintained at 3.5×10^{-10} mbar during insertion of a given photocathode sample via a transfer vessel and while performing XPS measurements. Ten minutes prior to photocathode insertion, the X-ray source is switched into operation mode to allow for a final degassing of the filament and pumping of the desorbed species in order to minimize photocathode contamination during analysis. The energy scale of the analyzer is regularly calibrated using sputter-cleaned polycrystalline Cu, Ag, and Au foils and characterizing the binding energy (BE) of the Cu2p$_{3/2}$, Ag3d$_{5/2}$ and Au4f$_{7/2}$ core levels as well as the Fermi edge.

The transfer vessel (a 3D model shown in Fig. 3) is equipped with a Ti-Zr-V non-evaporable getter (NEG) sputtered coating which allows for the transfer and transport of a photocathode, via a transfer arm, between the preparation chamber and the XPS machine under UHV conditions. The pressure in the NEG chamber (the bellows section in Fig. 3) of the vessel is always maintained below 1×10^{-11} mbar with the help of an ion pump which is separated from the connection flange with a gate valve, as shown in Fig. 3. The NEG activation is achieved by baking the NEG section at 230 °C for 24 h. Transfer of a photocathode into or from the preparation chamber or the XPS machine is achieved by first connecting and vacuum-sealing the connection flange to the given instrument, followed by baking the connection section at 150 °C for about two days under vacuum-pumping provided by an external turbo pump until the vacuum pressure is ~1×10^{-9} mbar. Subsequently, the gate valves linking the given instrument and the NEG chamber are opened allowing for photocathode transfer. The transfer arm of the transfer vessel holds the cathode plug during transport. The cathode plug remains on the transfer arm when introduced into the XPS analysis chamber. Using the integrated x-y-z manipulation of the transfer system, the arm is extended to the desired position and the sample surface is leveled to match the calibrated joint focus point of the electron analyzer and the X-ray source to maximize XPS intensity, which is in parallel recorded continuously.

3. Synthesis

The synthesis process starts with the substrate preparation. A cathode plug is turned, and polished with diamond powder in order to achieve an $\mathcal{R}_a < 0.02$ μm on the substrate surface [27,37], where $\mathcal{R}_a$ is the arithmetic average surface roughness parameter. A low $\mathcal{R}_a$ value is desired to limit field emission and any increase in geometrical beam emittance, a measure of the transverse momentum spread of the electron beam. The polished substrate is then degreased, and rinsed with distilled water followed by drying with clean compressed air. The cathode plug is then mounted inside the preparation chamber, vacuum-sealed, and the whole chamber is baked at ~150 °C for approximately four days to achieve UHV under vacuum pumping.

For the photocathodes reported here—labeled Cathodes 1–3 in chronological order of synthesis—the co-deposition synthesis procedure started with heating the substrate to a specific temperature followed by Sb deposition of ~3 nm. K vapor was then introduced on the deposited Sb while continuing the Sb deposition. Cs vapor was introduced as the third element. From the point forward of Cs introduction, all the three elements had been simultaneously deposited. The evaporation rate of a given element was controlled manually by the operator by adjusting the current driving the corresponding dispenser. Manual adjustments of dispenser currents allow for control over the stoichiometric ratio to a limited but certain extent. For all the photocathodes discussed here, the intended stoichiometry was CsK_2Sb. The deposition rates and durations were adjusted while monitoring the slope and maximizing the photocurrent measured in real time. A given synthesis procedure is stopped by utilizing the shutter when the in situ photocurrent peaks out despite adjustments to deposition rates (primarily alkali deposition rates). It is important to prevent a negative slope in the photocurrent which is attributed to the presence of excess of a chemical species and slower reaction rate of cathode formation, by avoiding any further deposition. Following termination of a deposition process, the cathode plug is quickly (~10 min) transferred to the DC gun for better vacuum environment via the transfer arm, and the plug temperature drops to room temperature due to natural heat loss to the ambiance over an expected period of a couple hours. During the deposition process, the pressure in the preparation chamber could rise up to ~5×10^{-7} mbar depending on the dispenser temperatures. The synthesis procedure is classified as a co-deposition procedure despite an initial sequential deposition due to its historical classification, e.g. see Ref. [26–28], and also because the photocurrent onsets during co-deposition of the elements under consideration. The initial Sb and K deposition is intended primarily to stabilize their rates prior to Cs deposition, for better control of the deposition rates of all the elements during the photocathode growth process.

The substrate temperature profiles, thicknesses, and the corresponding thickness growth rates and the evolution of the QEs during the syntheses of Cathodes 1–3 are shown in Fig. 4 (a)–(c), respectively. The thickness values shown in the plots were acquired at a rate of 4 Hz, using which the respective thickness growth rates were computed numerically in real time. For better visualization and without loss of validity, a 10-point moving average was applied for the thickness growth rates and QEs in the plots.

Since the synthesis duration and the QE evolution differ among photocathodes (depending on when the in situ photocurrent peaks out), only the regimes in the temporal proximity of the maximum QEs are displayed in Fig. 4. The time '0 (±1)' min corresponds to the end of the deposition process. The time values that approximately correspond to the beginning of addition of K and Cs vapors are shown as 'K addition' and 'Cs addition', respectively, in the corresponding plots in Fig. 4. It can be noted that Cathode 3, which has the highest QE $\simeq$ 6%, exhibits a longer evolution of QE resulting in a thicker photocathode relative to the other photocathodes that exhibit QEs ~ 2%, a trend consistent with our previous experiences with other high-QE semiconductor photocathodes like Cs-Te and Cs-Sb. However, a
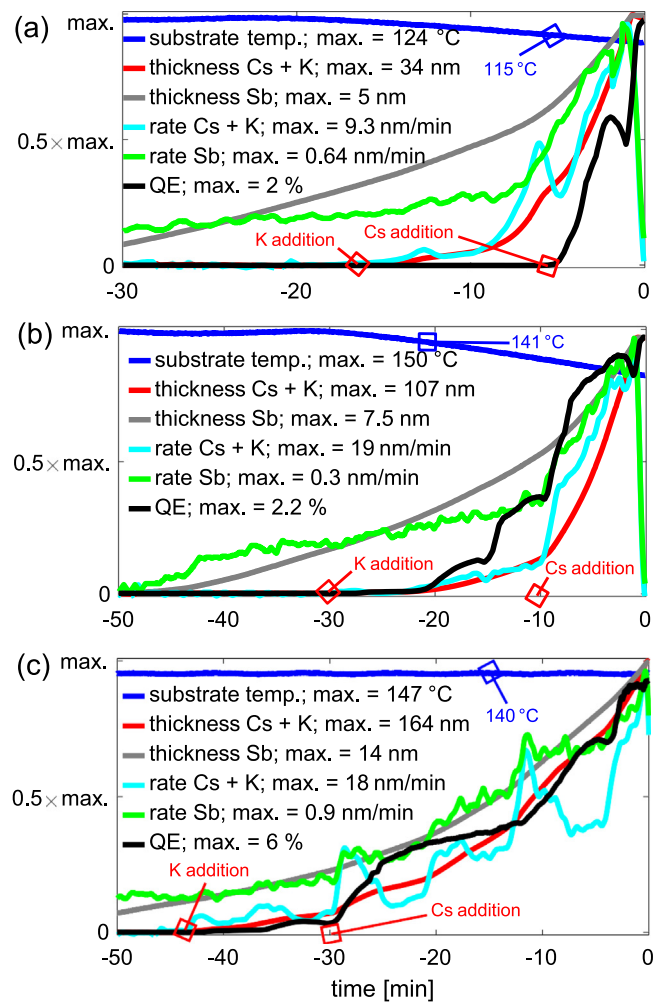

Fig. 4. Critical experimental parameters recorded during the synthesis of Cathode 1 (a), Cathode 2 (b) and Cathode 3 (c), where the dependency of the QE is shown as a function of the temperature and deposition parameters.

thicker photocathode does not necessarily yield a high QE if the QE evolution is slow or delayed subjected to non-optimal temperature or deposition rates. Experimentally each synthesis process may exhibit considerably different deposition parameters as a result of adjustment for maximizing the in situ measured photocurrent (or QE).

The temperature of the substrate dictates the subtle dynamics between the reaction rate of compound formation and the evaporation or displacement rate of an element already present on the substrate, while the available individual elemental fluxes influence the stoichiometry. While lower substrate temperatures induce slower reaction rates of cathode formation, higher temperatures induce faster evaporation or displacement rates of volatile metals, resulting in lower QEs. The externally set parameter chosen for the three photocathodes is the substrate temperature profile, while the deposition parameters are manually adjusted to follow the QE evolution dependent on the substrate temperature. For Cathodes 1 and 2, the substrate heating/temperature was not maintained during the synthesis process in order to avoid any electrical interference between the RF heater and the thickness monitors. For these two photocathodes, the RF heater was turned off once the corresponding desired temperature was reached just before the deposition process had begun. Consequently, the substrate temperature for Cathodes 1 and 2 decreased during the deposition process (ramped down profile) due to natural heat loss to the ambiance. For Cathode 3, the substrate was maintained at a constant temperature throughout the

deposition process by utilizing the RF heater since no interference was observed, after all.

Cs-K-Sb photocathode synthesis is known to be very sensitive to substrate temperature and deposition rates [37,38]. In Fig. 4 (a), a relatively low and ramped down substrate temperature profile ($T < 124$ °C) can be understood as the facilitator of a slower reaction rate resulting in a low QE while the deposition rates were manually optimized. In Fig. 4 (b), although initially $T \simeq 150$ °C, the temperature reduces to $T \sim 140$ °C at the onset of photocurrent and continues to decline to $T \sim 123$ °C towards the end of the deposition, likely aiding a low QE $\sim 2\%$ similar to that of Cathode 1. Apart from substrate effects which are discussed at the end of this Section, a relatively low QE arising from non-optimal combination of temperature and deposition rates results from improper stoichiometric ratio or excess of a chemical species [39]. In Fig. 4 (c), $T \simeq 140$ °C is maintained throughout the deposition process supporting a higher reaction rate resulting in a QE $\simeq 6\%$. It is important to note that a higher reaction rate calls for higher deposition rates when the slope of photocurrent is used as the driver for the photocathode growth process.

From Fig. 4, the overall thicknesses of Cathodes 1, 2 and 3 are estimated to be 39 nm, 114.5 nm and 178 nm, respectively. By comparing Cathodes 1 and 2, it can be noticed that although the QEs are similar, the thicknesses are quite different, emphasizing that the photocathode thickness is not the defining parameter in the current recipe as explained earlier in this Section. Within the limited set of trials incorporating our particular recipe, $T \sim 140$ °C has produced the highest QE, i.e $\sim6\%$. Owing to many orders of magnitude lower vapor pressure than those of Cs and K at the substrate temperatures under consideration, the effect of the substrate temperature on Sb evaporation is not seen as a concern. The analysis and results presented here are consistent with a previously reported detailed study of Cs-K-Sb photocathodes in Ref. [40], where photocathodes synthesized via sequential deposition methods at $T = 140$ °C resulted in highest QEs, with an average of 6.1%, compared to those synthesized at $T = 100$ °C and $T = 160$ °C for various deposition parameters. The substrate temperature utilized during alkali deposition in some other Cs-K-Sb synthesis recipes is also consistent with ~140 °C [37,41]. However, the reproducibility of obtaining reasonable QEs utilizing the current recipe remains to be further tested to gain statistical significance.

Recent Cs-K-Sb photocathode preparation systems incorporate precise control of individual deposition rates of all elements being deposited towards obtaining a desired stoichiometry, sometimes incorporating in situ X-ray based diagnostics [31,42]. The photocathode synthesis results presented herein offer a viable synthesis procedure to synthesize Cs-K-Sb photocathodes using an improved but conventional apparatus despite its inherited limitations. Although there is no precise control or diagnosis of in situ stoichiometry during photocathode fabrication, optimization of QE by adjustments to individual dispenser currents allows for a limited control over stoichiometry. The effectiveness of the geometric design of the preparation chamber depicted in Fig. 2 in producing circularly symmetric deposition is demonstrated in Fig. 5, where the spatial variation of the QE for the three photocathodes is shown.

It can be easily seen that the average stoichiometric ratio of two elements 'a' and 'b' can be given as $r_{a:b} = (k_a \rho_a m_b)/(k_b \rho_b m_a)$, where k is the deposited thickness, ρ is the elemental density and m is the elemental atomic mass—corresponding to the elements in the suffixes. However, estimation of such a ratio was not feasible in the current case since the deposition thickness for Cs and K are individually not known. It should be noted that the precision on the quartz thickness monitors is difficult to estimate due to lack of reliable alternative high-precision apparatus and methods at a nanometer-scale. Instead, an estimation of composition ratio by XPS measurements is addressed in Section 5.

Copper substrates: In a previously conducted study, Cs-K-Sb photocathodes synthesized on Cu substrates yielded QE $\sim 0.2\%$, while those synthesized on stainless steel substrates yielded QE $\sim 2\%$ at
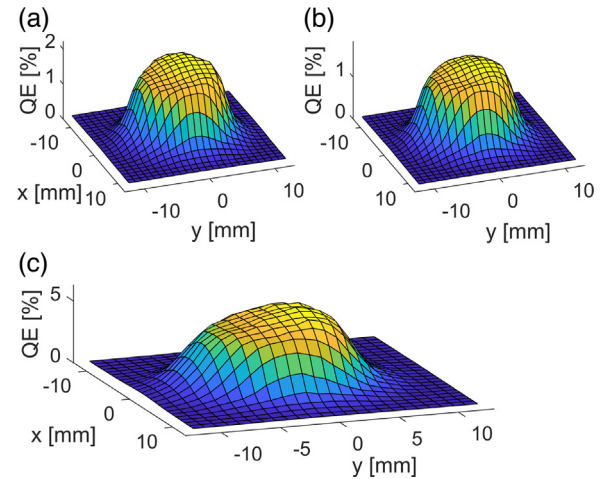

Fig. 5. 3D plots of the spatial variation of the QE for Cathode 1 (a), Cathode 2 (b) and Cathode 3 (c), where 'x' and 'y' correspond to the Cartesian planar coordinates of a given photocathode surface. The QE scans were obtained at a resolution of one data point per mm^2 area, while each data point was an average of 25 consecutive readings of QE acquired at a laser repetition rate of 10 Hz.

532-nm laser wavelength under similar conditions [43]. It was also shown that a rougher Cu substrate surface yields significantly less QE, possibly due to increased diffusion of Cu into Sb. Nevertheless, the experimental and photocathode conditions utilized in the study were vastly different from those reported herein: (i) the study employed a sequential deposition procedure in the order Sb, K and Cs which may be more prone to Cu diffusion into Sb, (ii) the surface roughness of the Cu substrate used in the study corresponds to $\mathcal{R}_a \sim 1$ µm in contrast to $\mathcal{R}_a < 0.02$ µm in the current studies, (iii) the thicknesses of Cathodes 2 and 3 are significantly larger than those of the photocathodes reported in the study (likely <100 nm). These factors, combined with the XPS analysis on Cathode 3 reported in Section 5 where no Cu contamination has been found on the photocathode surface, may explain the vast differences in the QE results between the two studies. Another study found that Cs-K-Sb photocathodes synthesized on Cu, Mo, and stainless steel substrates yielded similar QEs ($\approx2\%$ at 542-nm laser wavelength) [44]. Furthermore, previously reported XPS data on Cs-Sb photocathodes synthesized on similar Cu substrates showed no Cu contamination on the photocathode surfaces [27,28], supporting the suitability of Cu substrates for alkali antimonide photocathodes. High thermal conductivity of Cu offers effective heat dissipation from photocathodes which is important for continual operation.

4. Lifetime studies

The charge-lifetime (τ_Q) of a photocathode is an appropriate figure of merit to quantify the longevity of a photocathode, normally defined as the total charge that can be extracted until the QE is reduced to $1/e$ times the initial QE under a constant current density of extraction. τ_Q is a convenient photocathode performance indicator under continuous wave or pulsed laser illumination.

If α_i represent distinct parameters like extraction time and emitted-charge density that affect the quantum yield, where $i \in \{1, 2, \dots, l\}$ and $l \in \mathcal{Z}^+$, then the QE, η, can be generally given in terms of the initial QE, η_0, as

$$\eta(\alpha_1, \dots, \alpha_l) = \eta_0 \prod_{i=1}^{l} e^{-\frac{\alpha_i}{\tau_i}}, \tag{1}$$

where τ_i are the 'lifetimes' corresponding to α_i. Eq. (1) assumes absence of coupling among α_i. In practice, there are several critical factors like vacuum pressure, chemical environment, current density, laser wavelength and initial QE that influence photocathode degradation. In
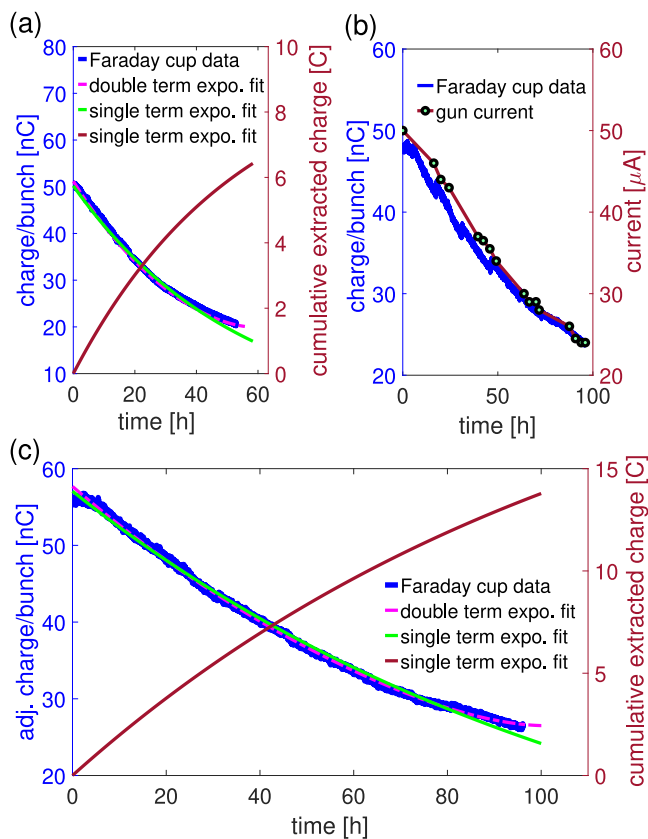
Fig. 6. Bunch charge evolution in time (t) for an oxidized state of Cathode 2 (a), raw data for an oxidized state of Cathode 3 (b) and calibrated (adjusted) data of the same (c).

Table 1

Some important experimental, fitted and extracted parameters from Fig. 6, where R^2 is the coefficient of fit-determination, $\bar{I}_0$ is the average current, $\hat{I}_0$ is the peak current, $\hat{j}_0$ is the peak current density at the beginning of the lifetime studies ($t = 0$), E is the laser pulse energy, σ is the laser spot size, $\mathcal{I}$ is the laser pulse intensity and p is the pressure in the DC gun. The coefficients and exponents in the fit equations are rounded to two decimal places.

Case	Fig. 6 (a) (Cathode 2)	Fig. 6 (c) (Cathode 3)
1-term fit	$50.21e^{-0.02t}$	$57.06e^{-0.01t}$
std. error, R^2	0.6634, 0.9945	0.5963, 0.9958
2-term fit	$51e^{-0.02t} + 0.19e^{0.06t}$	$57.67e^{-0.01t} + 0.01e^{0.06t}$
std. error, R^2	0.2934, 0.9989	0.3656, 0.9984
τ_t [h]	~53.68	~116.44
τ_Q [C]	~6.13	~13.78
η_0 [%]	0.28	2.5
$\bar{I}_0$ [μA]	51	56.5
$\hat{I}_0$ [A]	1	1.1
$\hat{j}_0$ [A/mm^2]	0.07	0.08
E [μJ]	41.6	5.2
σ, rmsd [mm]	2.1	2.1
$\mathcal{I}$ [W/mm^2]	60	7.5
p [mbar]	~2.7×10^{-11}	~2.0×10^{-11}

reference to Eq. (1), the $1/e$ lifetime (τ_t) is defined from $\eta(t) = \eta_0 e^{-\frac{t}{\tau_t}}$, and $\tau_Q = \int_0^{\tau_t} I(t)dt$, where t is time and I is current.

In order to analyze photocathode longevity under high peak current extraction rates (ampere-level), lifetime studies on Cathode 2 and Cathode 3 were carried out by illumination with 1-kHz (50 ns fwhm) laser repetition rate at 532-nm wavelength for several days while extracting several tens of nC charge per bunch in the DC gun; some additional laser pulse specifications are listed in Table 1.

It is to be noted that at the beginning of the lifetime studies, both photocathodes were in degraded states of QE resulting from oxidation due to either transient poor vacuum conditions related to beam characterization experiments (for Cathode 2) or residual gas molecules in the XPS system (for Cathode 3); the initial QEs (η_0) of the photocathodes are shown in Table 1. Fig. 6 shows the evolution of the charge per bunch for both photocathodes, which is proportional to the QE, as a function of time. The charge was emitted from the electrostatic center of the DC gun since any off-center emitting positions resulted in considerable particle loss in the beam transport. For the sake of experimental simplicity, the drive laser energy was maintained constant during photocathode illumination as a result of which the current bore a nonconstant profile. The raw data corresponding to Cathode 3 in Fig. 6 (b) includes discontinuities in the charge per bunch values with time, whose source of origin is unclear. In order to rectify the effects of these discontinuities, the FC data was adjusted after cross calibrating with the gun current (Fig. 6 (b) right-hand side plot) as shown in Fig. 6 (c), since the FCT was under overhaul. The initial plateau seen in the charge–time data in Fig. 6 (c) is attributed to the desorption period of the gas introduced in the XPS chamber.

The fit parameters and some other important extracted experimental data from Fig. 6 are compiled in Table 1. In each of Fig. 6 (a) and (c), the right-hand side plot shows the respective evolution of the extracted

charge as a function of time based on the corresponding single-term exponential fit. Unlike in the plots shown in Fig. 6, in some cases, the lifetime curves exhibit visually distinct double exponential decay in which case a two-term exponential fit may be incorporated. Such a decay may be seen as a superposition of two exponential decay processes corresponding to extraction time t. In each of Fig. 6 (a) and (c), the double-term exponential fit with dashed-line, where one of the terms results in a positive exponent (see Table 1), is shown only for reference and comparison with the single-term fit. A process pertaining to such a double-term fit may be ignored for large t since the positive exponential term grows with t contrary to experimental observations. Moreover, the fits are applicable to limited data ranges. Anomalies from a clear exponential decay of charge arise from coupled decay processes corresponding to α_i in Eq. (1). For instance, a modified and validated Langmuir model for adsorption of gases which additionally incorporates irreversible reaction of contaminating gases with the photocathode surface, explains deviation of charge–time curves from single exponential decay [45]. In each case, it can be noted that the coefficient of the positive exponent term in the double-exponential fit is minuscule compared to that of the negative exponent term, which warrants the adequacy of a single-exponential fit for an approximate estimation of charge-lifetime.

It may be noted that the QE degradation is more dramatic under high laser intensities due to laser induced thermal effects, independent of extracted beam current [46–48]. Corresponding to a degraded η_0 of 2.5% (due to oxidation) and photoemission from the electrostatic center of the DC gun, the ~13.78-C estimated charge-lifetime of Cathode 3 is generally in line with that of order of 10 C under mA average DC currents found in some literature [8]. While oxidation of these photocathodes plays a major role in lifetime degradation due to chemical changes, the electrostatic centers of Cs-K-Sb and Ga-As photocathodes are known to undergo significant surface damage due to ion bombardment [8,16,49]. Although it is difficult to make direct comparisons among photocathodes characterized under different experimental conditions, charge-lifetimes as high as thousands of coulomb have been claimed by data extrapolation from pristine Cs-K-Sb photocathodes under off-electrostatic-center photoemission in Ref. [16].

5. Surface chemical composition analysis

The surface chemical composition and bond configuration of Cathode 3 were examined before and after the lifetime studies via XPS. Data analysis and peak fitting were performed utilizing CasaXPS v.2.3.19
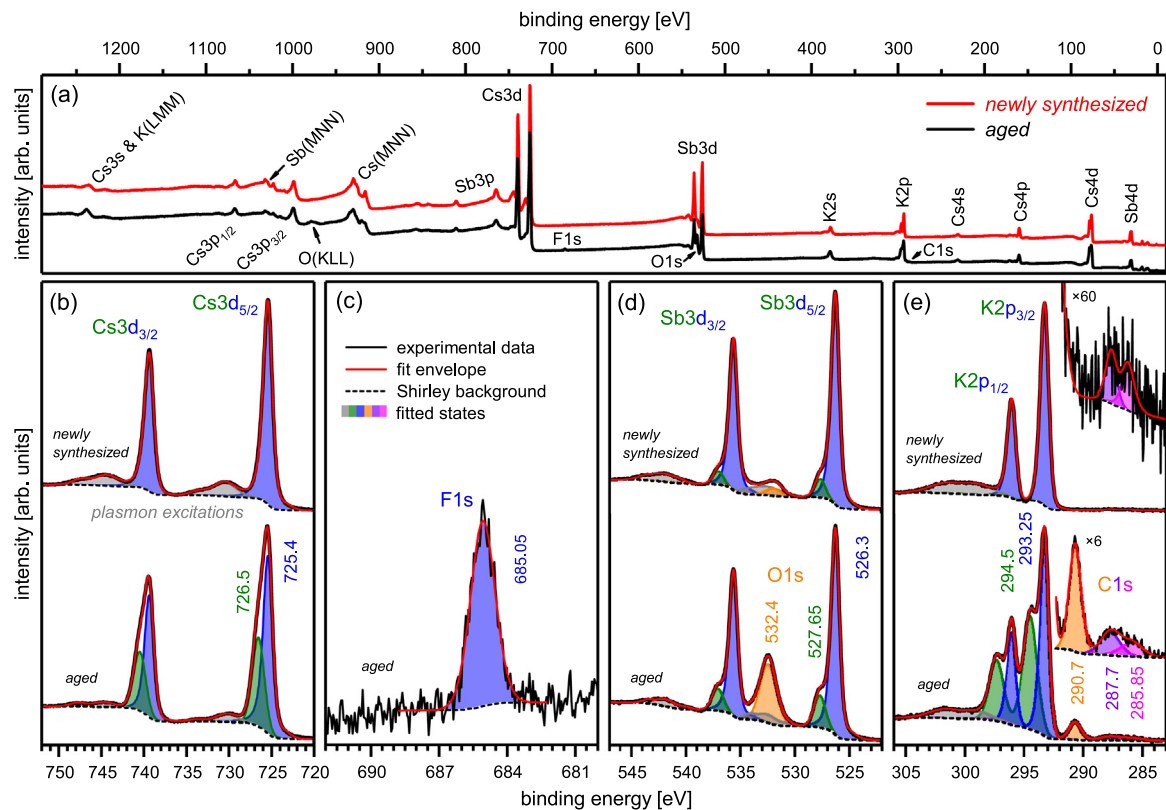
Fig. 7. XPS spectra of Cathode 3 as newly synthesized and after ageing: survey spectra with assignment of the detected photoelectron and Auger-electron lines (a), high-resolution core level spectra of the Cs3d, F1s, Sb3d & O1s, K2p & C1s states, respectively, in order of increasing (decreasing) kinetic (binding) energy scale (b)–(e). The individual core level fits include different chemical states and spin–orbit splitting of the single elements, superposition of different states as well as contributions from inelastically scattered electrons that underwent energy loss due to excitation of plasmons within the material as indicated by the color-coded assignment. (For interpretation of the references to color in this figure legend, the reader is referred to the web version of this article.)

(Casa Software Ltd., UK) using Gaussian–Lorentzian line shapes and Shirley-type background subtraction, and considering fixed spin–orbit splitting energies and the corresponding doublet features having the same full width at half maximum (FWHM). Besides, only one further constraint was used for least-square fitting of the spectra: the FWHM of the Cs3d main chemical component (states marked in blue in Fig. 7 (b)) of the aged sample was fixed to the FWHM value obtained for the newly synthesized sample.

Fig. 7 compares the XPS spectra of Cathode 3 as newly synthesized and after ageing, i.e. after the lifetime studies. The major signals of the detected elements are assigned in Fig. 7 (a), including the states originating from Cs, K, Sb, O, and C. In addition, some adsorbates of F were detected after ageing. The main core level spectra of the specific elements are plotted in Fig. 7 (b)–(e). For the attribution of chemical states, it is helpful to also consider the quantitative contribution of each element. To calculate the surface elemental composition, we considered the spectral areas of the main core level of each detected element and weighted them with their respective sensitivity factors. The sensitivity factors were estimated by considering the corresponding cross-sections of photoelectron generation [50], the inelastic mean free paths estimated based on the TPP-2M model [51], and the analyzer transmission function for the implemented experimental settings (based on Monte Carlo simulations provided by SPECS Surface Nano Analysis GmbH, Berlin, Germany). A model of homogeneous composition of all detected elements—which slightly overestimates the contribution of a species located at the outermost surface, such as adsorbates—was applied [52]. The corresponding compositions before and after ageing are listed in Table 2 together with the relative chemical state contributions within each core level.

For analysis and deconvolution of the individual components, especially in the alkali core level spectra, the contributions from satellite

lines due to excitation of plasmons (gray spectral features in Fig. 7 (b), (d) and (e)) within the material have to be considered as well as the spin–orbit splitting of the p and d electrons [53]. For the newly synthesized photocathode surface, the Cs3d and K2p spectra include solely one chemical state (Cs3d$_{5/2}$ peak at 725.4 eV and K2p$_{3/2}$ at 293.2 eV), while the main Sb3d$_{5/2}$ line at 526.3 eV exhibits a slightly high BE shoulder at 527.7 eV. The origin of these features has already been discussed in earlier studies on comparable photocathodes [28,41, 42,54]. According to those references, the chemical components are related to ionized K$^+$ and Cs$^+$ species and Sb^{3-} formed via charge transfer from the alkali atoms. The Sb3d side shoulder is attributed to neutral Sb^0 or Sb in a lower oxidation state (Sb^{x-}, with $x < 3$) [55] which could be linked to a slight excess of Sb during growth since the BE of oxide phases is typically higher [56,57]. In addition, only minor surface impurities (O and hydrocarbons from residual gas adsorption) were detected, verifying the efficiency of the UHV transfer of this highly reactive material. Furthermore, the intense plasmon loss features in the core level spectra are qualitative fingerprints of a high-purity material with optimized electronic properties for photoemission.

After ageing, a significant change in the surface composition was evident. A strong oxidation of the surface occurred: the O content increased to 23.0 at.% and high BE oxide-related features [58–60] appeared in the Cs3d$_{5/2}$ and K2p$_{3/2}$ core level spectra (Fig. 7 (b) and (e)) at 726.5 eV and 294.5 eV, respectively. It is interesting to note that the fraction of the two different oxidation states of Sb did not change substantially (only a small increase of the component at 527.65 eV occurred, which is in agreement with observations from an earlier study [55]) and that no oxidation of Sb surface atoms occurred, while past studies of other photocathode materials reported on Sb oxidation [28,57]. Consequently, most of the charge transfer with the O atoms was mediated by the alkali surface atoms. Furthermore,

Table 2

Results from quantitative analysis of the XPS data in Fig. 7 including the individual relative contents of chemical states contributing to each core level spectrum as well as the surface composition (in at. %) based on quantitative analysis.

Element + state	State BE [eV]	Newly synthesized cathode		Aged cathode	
		Relative contribution [%]	Composition [at. %]	Relative contribution [%]	Composition [at. %]
$Cs3d_{5/2}$	726.5	–	30.3	38.3	18.2
	725.4	100		61.7	
$Sb3d_{5/2}$	527.7	9.4	23.6	16.7	11.1
	526.3	90.6		83.3	
$K2p_{3/2}$	294.5	–	43.3	50.5	39.2
	293.2	100		49.5	
O1s	532.4	100	2.3	100	23.0
C1s	290.7	–	0.6	63.9	7.3
	287.7	47.1		21.3	
	285.8	52.9		14.8	
F1s	685.1	–	–	100	1.2

adsorption of carbon-related surface impurities with distinct C1s states at 290.7, 287.7 and 285.8 eV was observed. The major contribution at 290.7 eV originates from surface reactions with species from residual gases and could either be induced by carbonate formation via interaction with CO_2 [28] or via adsorption of F species forming CF_2 bonds [61]. In parallel, an F1s signal equivalent to 1.2 at. % of surface F impurities was detected after photocathode aging. RGA measurements of the preparation chamber confirmed the presence of minor F contents in the vacuum system, which is suspected to arise from a Viton® vacuum gasket in the DC gun beamline that was accidentally overheated during a baking process several years ago.

A further observation after ageing was the intensity reduction of the plasmon-loss-induced spectral signatures. This effect points towards an attenuation of the possibility to excite collective phenomena at the material surface due to disorder or contamination, which is linked to an intrinsic reduction of QE. The primary chemical effect appears to be the oxidation of the surface alkali atoms during lifetime studies when the photocathode is continuously illuminated with a high peak-intensity laser at high repetition rates. The photo-excitation of the electrons in the material has the potential to 'catalyze' or enhance reactions of the surface with molecules from the residual gases of the vacuum chamber, and especially to enhance the affinity to O, water and CO_x dissociation and adsorption [62,63]. It is further anticipated that the surface oxidation enhances the work function and ionization potential of the photocathode material thus increasing the barrier for photon-induced electron emission processes [60,64] with direct impact on the QE.

6. Summary and conclusions

A total of three Cs-K-Sb photocathodes have been synthesized on copper substrates via a ternary co-deposition method with the slope of photocurrent as the driver, using a preparation system that was originally designed for synthesis of two-element compounds. Gearing towards maximizing the QE, the substrate temperatures and deposition parameters were varied during synthesis among three photocathodes labeled Cathode 1, Cathode 2, and Cathode 3, viz., ramped down $T \simeq 124\ °C$, ramped down $T \simeq 150\ °C$, and a constant $T \simeq 140\ °C$, respectively. A maximum QE of 6% at 532-nm laser wavelength obtained for Cathode 3 is consistent with certain previously conducted studies corresponding to sequential layered deposition methods. The reproducibility of the Cs-K-Sb synthesis recipe followed here is to be further tested in detail for statistical significance.

Lifetime studies of oxidized Cathodes 2 and 3 under ampere-level peak currents and tens of micro-ampere average currents, emitted from electrostatic center, driven by a 532-nm wavelength, 1-kHz repetition rate laser yielded charge-lifetimes of ~6.13 C and ~13.78 C corresponding to the degraded initial QEs of 0.28% and 2.5% owing to

significant oxidation, and $1/e$ lifetimes of ~53.68 h and ~116.44 h, respectively. The results suggest that Cs-K-Sb photocathodes are operable at kHz repetition rates and at tens of nC/bunch charge extraction in DC gun environments. These outcomes, if can be improved and tested for RF gun environments, are important in regard to the generation of high brightness beams for superconducting RF linacs and future electron colliders where several nC/bunch at ps-level durations may be desired. Intrinsic emittance and surface roughness measurements (scanning tunneling microscopy) of Cs-K-Sb (along with Cs-Te) photocathodes emanating from the recipe followed in the current studies is underway under a collaboration between CERN and the Science and Technology Facilities Council (STFC), Daresbury Laboratory (UK).

XPS analysis performed before the lifetime studies on Cathode 3 revealed a clean photocathode surface as synthesized. The quantitative XPS analysis yielded a compositional ratio of $Cs_{1.3}K_{1.8}Sb$, hence slightly Cs-rich compared to the nominal composition of the CsK_2Sb phase. The operation of this photocathode in the test beamline under laser illumination induced strong oxidation of the alkali atoms at the surface resulting in a 23.0 at. % surface O uptake. The persistent irradiation and high peak current electron emission possibly further induced adsorption of C (7.3 at. %) and traces of F (1.2 at. %) from the residual gases of the DC gun beamline. Active photocathode cooling and designing higher thermal conductivity photocathodes can mitigate laser induced thermal effects under high intensity and repetition rates. Additionally, technical efforts to reduce the partial pressures of the remaining residual gases in the XPS machine and limiting the XPS measurement time, at the cost of signal-to-noise-ratio, should significantly improve Cs-K-Sb photocathode lifetime.

CRediT authorship contribution statement

H. Panuganti: Conceptualization, Formal analysis, Writing - original draft. **E. Chevallay:** Methodology, Validation. **V. Fedosseev:** Supervision, Project administration. **M. Himmerlich:** Formal analysis, Writing - original draft.

Declaration of competing interest

The authors declare that they have no known competing financial interests or personal relationships that could have appeared to influence the work reported in this paper.

Acknowledgments

References

[1] K.L. Jensen, Advances in Imaging and Electron Physics, Vol. 149, Elsevier Academic Press, San Diego, 2007.

[2] H. Panuganti, P. Piot, Observation of two-photon photoemission from cesium telluride photocathodes excited by a near-infrared laser, Appl. Phys. Lett. 110 (2017) 093505.

[3] M. Petrarca, M. Martyanov, M. Divall, G. Luchinin, Study of the Powerful Nd:YLF Laser Amplifiers for the CTF3 Photoinjectors, IEEE J. Quantum Electron. 47 (3) (2011) 306–313.

[4] L. Liu, Y. Du, B. Chang, Q. Yunsheng, Spectral response variation of a negative-electron-affinity photocathode in the preparation process, Appl. Opt. 45 (24) (2006) 6094–6098.

[5] C. Krantz, Intense Electron Beams from GaAs Photocathodes As a Tool for Molecular and Atomic Physics (Doctoral Dissertation), Ruperto-Carola University of Heidelberg, Germany, 2009.

[6] Y. Honda, S. Matsuba, X. Jin, T. Miyajima, M. Yamamoto, T. Uchiyama, M. Kuwahara, Y. Takeda, Temporal response measurements of GaAs-based Photocathodes, Japan. J. Appl. Phys. 52 (2013) 086401.

[7] A.V. Aleksandrov, et al., Experimental study of the response time of GaAs as a photoemitter, Phys. Rev. E 51 (1995) 1449.

[8] R.R. Mammei, et al., Charge lifetime measurements at high average current using a K_2CsSb photocathode inside a dc high voltage photogun, Phys. Rev. Spec. Top. - Accel. Beams 16 (2013) 033401.

[9] A.H. Sommer, Photoemissive Materials, John Wiley & Sons, New York, 1980.

[10] W.E. Spicer, Photoemissive, photoconductive, and optical absorption studies of Alkali-Antimony compounds, Phys. Rev. 112 (1958) 114.

[11] L. Cultrera, C. Gulliford, A. Bartnik, H. Lee, I. Bazarov, Rb based alkali antimonide high quantum efficiency photocathodes for bright electron beam sources and photon detection applications, J. Appl. Phys. 121 (2017) 055306.

[12] D.E. Persyk, J. Morales, R. McKeighen, G. Muehllehner, The Quadrant photomultiplier, IEEE Trans. Nucl. Sci. 26 (1) (1979) 364–367.

[13] A. Sommer, Conventional and negative electron affinity photoemitters, J. Phys. Colloq. 34 (C6) (1973) 51–60.

[14] T. Rao, et al., Photocathodes for the energy recovery linacs, Nucl. Instrum. Methods Phys. Res. A 557 (1) (2006) 124–130.

[15] T. Vecchione, I. Ben-Zvi, D.H. Dowell, J. Feng, T. Rao, J. Smedley, W. Wan, H.A. Padmore, A low emittance and high efficiency visible light photocathode for high brightness accelerator-based X-ray light sources, Appl. Phys. Lett. 99 (2011) 034103.

[16] B. Dunham, et al., Record high-average current from a high-brightness photoinjector, Appl. Phys. Lett. 102 (2013) 034105.

[17] I. Bazarov, L. Cultrera, A. Bartnik, B. Dunham, S. Karkare, Y. Li, X. Liu, J. Maxson, W. Roussel, Thermal emittance measurements of a cesium potassium antimonide photocathode, Appl. Phys. Lett. 98 (2011) 224101.

[18] C. Cocchi, S. Mistry, M. Schmeißer, J. Kühn, T. Kamps, First-principles many-body study of the electronic and optical properties of CsK_2Sb, a semiconducting material for ultra-bright electron sources, J. Phys.: Condens. Matter 31 (2019) 014002.

[19] K.-H. Jang, K. Oang, I. Baek, S. Setiniyaz, K. Lee, Y. Jeong, H. Kim, Ultrafast electron diffraction technology for exploring dynamics of Molecules, J. Korean Phys. Soc. 73 (4) (2018) 466–478.

[20] S.P. Weathersby, et al., Mega-electron-volt ultrafast electron diffraction at SLAC National Accelerator Laboratory, Rev. Sci. Instrum. 86 (2015) 073702.

[21] P.N. Burrows, P. Lebrun, L. Linssen, D. Schulte, E. Sicking, S. Stapnes, M.A. Thomson, Updated Baseline for a Staged Compact Linear Collider, CERN-2016-004, 2016.

[22] P. Lebrun, L. Linssen, A. Lucaci-Timoce, D. Schulte, F. Simon, S. Stapnes, N. Toge, H. Weerts, J. Wells (Eds.), The CLIC Programme: Towards a Staged e^+e^- Linear Collider Exploring the Terascale, CLIC Conceptual Design Report, CERN-2012-005, 2012.

[23] H.H. Braun, E. Chevallay, S. Hutchins, P. Legros, G. Suberlucq, H. Trautner, I.N. Ross, E. Bente, The photo-injector option for CLIC: Past experiments and future developments, in: Proceedings of the 2001 Particle Accelerator Conference, Chicago, IL, USA, 2001, pp. 720–722.

[24] O. Mete, E. Chevallay, M. Csatari, A. Dabrowski, S. Doebert, D. Egger, V. Fedosseev, M. Olvegaard, M. Petrarca, Production of long bunch trains with 4:5 μC total charge using a photoinjector, Phys. Rev. Spec. Top. - Accel. Beams 15 (2012) 022803.

[25] M. Csatari Divall, et al., Fast phase switching within the bunch train of the PHIN photo-injector at CERN using fiber-optic modulators on the drive laser, Nucl. Instrum. Methods Phys. Res. A 659 (1) (2011) 1–8.

[26] C. Hessler, E. Chevallay, S. Doebert, V. Fedosseev, I. Martini, M. Martyanov, Recent results on the performance of Cs_3Sb photocathodes in the PHIN RF-Gun, in: Proceedings of the 6th International Particle Accelerator Conference, Richmond, VA, USA, 2015, pp. 1699–1702.

[27] I. Martini, Characterization of Cs-Sb Cathodes for High Charge RF Photoinjectors (Doctoral Dissertation), Politechnico di Milano, Italy, 2015.

[28] I. Martini, E. Chevallay, V. Fedosseev, C. Hessler, H. Neupert, V. Nistor, M. Taborelli, X-ray photoemission spectroscopy studies of Cesium Antimonide Photocathodes for Photoinjector applications, Physics Procedia 77 (2015) 34–41.

[29] E. Prat, S. Bettoni, H. Braun, R. Ganter, T. Schietinger, Measurements of copper and cesium telluride cathodes in a radio-frequency photoinjector, Phys. Rev. Spec. Top. - Accel. Beams 18 (2015) 043401.

[30] C. Ghosh, B.P. Varma, Preparation and study of properties of a few alkali antimonide photocathodes, J. Appl. Phys. 49 (1978) 4549.

[31] Z. Ding, M. Gaowei, J. Sinsheimer, J. Xie, S. Schubert, H. Padmore, E. Muller, J. Smedley, In-situ synchrotron x-ray characterization of K_2CsSb photocathode grown by ternary co-evaporation, J. Appl. Phys. 121 (2017) 055305.

[32] J. Feng, S. Karkare, J. Nasiatka, S. Schubert, J. Smedley, Near atomically smooth alkali antimonide photocathode thin films, J. Appl. Phys. 121 (2017) 044904.

[33] E. Chevallay, Experimental Results at the C.E.R.N. Photoemission Laboratory with Co-Deposition Photocathodes in the Frame of the CLIC Studies, CERN CTF3 Note 104, 2012.

[34] J. Durand, T. Tardy, M. Wurgel, A 10 GHz Wall Current Monitor, CERN PS/LP/Note 95-09, 1995.

[35] G. Suberlucq, Technological challenges for high brightness photo-injectors, in: Proceedings of the 9th European Particle Accelerator Conference, Lucerne, Switzerland, 2004, pp. 64–68.

[36] J. Teichert, R. Xiang, G. Suberlucq, J. Verschuur, Report on Photocathodes, CARE Note-2004-033-PHIN, 2004.

[37] D.H. Dowell, S.Z. Bethel, K.D. Friddell, Results from the average power laser experiment photocathode injector test, Nucl. Instrum. Methods Phys. Res. A 356 (2–3) (1995) 167–176.

[38] S. Schubert, S. Karkare, et al., Bi-alkali antimonide photocathode growth: An X-ray diffraction study, J. Appl. Phys. 120 (2016) 035303.

[39] C. Cocchi, S. Mistry, M. Schmeißer, R. Amador, J. Kühn, T. Kamps, Electronic structure and core electron fingerprints of caesium-based multi-alkali antimonides for ultra-bright electron sources, Sci. Rep. 9 (2019) 18276.

[40] R.L. Ternes, S.Z. Bethel, D.G. Janky, A statistically-designed experiment for assessing cesium-potassium-antimonide photocathode fabrication parameters, Nucl. Instrum. Methods Phys. Res. A 318 (1) (1992) 401–409.

[41] S. Schubert, J. Smedley, et al., Bi-alkali antimonide photocathodes for high brightness accelerators, APL Mater. 1 (2013) 032119.

[42] M.A.H. Schmeißer, S. Mistry, H. Kirschner, S. Schubert, A. Jankowiak, T. Kamps, J. Kühn, Towards the operation of Cs-K-Sb photocathodes in superconducting rf photoinjectors, Phys. Rev. Accel. Beams 21 (2018) 113401.

[43] J. Smedley, T. Rao, E. Wang, K_2CsSb cathode development, in: Proceedings of the 18th International Spin Physics Symposium, Newport News, VA, USA, 2009, pp. 1062–1066.

[44] A. Burrill, I. Ben-Zvi, T. Rao, D. Pate, Z. Segalov, D. Dowell, Multi-Alkali photocathode development at brookhaven national lab for application in superconducting photoinjectors, in: Proceedings of the 2005 Particle Accelerator Conference, Knoxville, TN, USA, 2005, pp. 2672–2674.

[45] V. Pavlenko, F. Liu, M.A. Hoffbauer, N.A. Moody, E.R. Batista, Kinetics of alkali-based photocathode degradation, AIP Adv. 6 (2016) 115008.

[46] E. Riehn, V. Tioukine, K. Aulenbacher, Lifetime measurements of DBR And non-DBR photocathodes at high laser intensities, in: Proceedings of the 13th International Workshop on Polarized Sources, Targets and Polarimetry, Ferrara, Italy, 2009, pp. 241–248.

[47] K. Aulenbacher, Polarized beams for electron accelerators, Eur. Phys. J.: Spec. Top. 198 (2011) 361–380.

[48] V. Bechthold, K. Aulenbacher, M.A. Dehn, S. Friederich, Investigation of K_2CsSb photocathodes, in: Proceedings of the 59th ICFA Advanced Beam Dynamics Workshop on Energy Recovery Linacs, Geneva, Switzerland, 2017, pp. 4–8.

[49] L. Cultrera, et al., Photocathode behavior during high current running in the Cornell energy recovery linac photoinjector, Phys. Rev. Spec. Top. - Accel. Beams 14 (2011) 120101.

[50] J.J. Yeh, I. Lindau, Atomic subshell photoionization cross sections and asymmetry parameters: $1 \leq Z \leq 103$, At. Data Nucl. Data Tables 32 (1) (1985) 1–155.

[51] S. Tanuma, C.J. Powell, D.R. Penn, Calculation of electron inelastic mean free paths (IMFPs) VII. Reliability of the TPP-2M IMFP predictive equation, Surf. Interface Anal. 35 (3) (2003) 268–275.

[52] M.P. Seah, The quantitative analysis of surfaces by XPS: A review, Surf. Interface Anal. 2 (6) (1980) 222–239.

[53] J.F. Moulder, W.F. Stickle, P.E. Sobol, K.D. Bomben, Handbook of X-Ray Photoelectron Spectroscopy, Perkin-Elmer Corporation, Eden Prairie, 1992.

[54] S. Schubert, J. Smedley, T. Rao, M. Ruiz-Oses, X. Liang, I. Ben-Zvi, H. Padmore, T. Vecchione, XPS and UHV-AFM analysis of the K_2CsSb-photocathode growth, in: Proceedings of the 4th International Particle Accelerator Conference, Shanghai, China, 2013, pp. 291–293.

[55] C.W. Bates Jr., Th.M. van Atekum, G.K. Wertheim, D.N.E. Buchanan, K.E. Clements, X-ray photoemission studies of superficially oxidized cesium antimonide photoemitters, Appl. Phys. Lett. 38 (1981) 387–389.

[56] F. Garbassi, XPS and AES study of antimony oxides, Surf. Interface Anal. 2 (5) (1980) 165–169.

[57] L. Soriano, L. Galán, Interaction of Cesium-Potassium Antimonide Photocathode Materials with Oxygen: an X-ray Photoelectron Spectroscopy study, Japan. J. Appl. Phys. 32 (1993) 4737–4744.

[58] C.Y. Su, I. Lindau, P.W. Chye, S.-J. Oh, W.E. Spicer, Photoemission studies of clean and oxidized Cs, J. Electron Spectrosc. Relat. Phenom. 31 (3) (1983) 221–259.

[59] B. Lamontagne, F. Semond, D. Roy, K overlayer oxidation studied by XPS: the effects of the adsorption and oxidation conditions, Surf. Sci. 327 (1995) 371–378.

[60] V. Irkha, A. Himmerlich, S. Reiß, S. Krischok, M. Himmerlich, Effects of Potassium Adsorption and Potassium–Water coadsorption on the chemical and electronic properties of n-Type GaN(0001) Surfaces, J. Phys. Chem. C 122 (8) (2018) 4250–4260.

[61] M. Himmerlich, V. Yanev, A. Opitz, A. Keppler, J.A. Schaefer, S. Krischok, Effects of X-ray radiation on the surface chemical composition of plasma deposited thin fluorocarbon films, Polym. Degrad. Stab. 93 (3) (2008) 700–706.

[62] H.P. Bonzel, G. Pirug, A. Winkler, Adsorption of H_2O on potassium films, Surf. Sci. 175 (2) (1986) 287–312.

[63] J.R. Hoenigman, R.G. Keil, An XPS study of the adsorption of oxygen and water vapor on clean lithium films, Appl. Surf. Sci. 18 (1–2) (1984) 207–222.

[64] G.E. Rhead, On the work function variations produced by the oxidation of adsorbed alkali metal layers, Appl. Surf. Sci. 47 (1) (1991) 35–42.